

# Chapter 1

## Measurement of the Left-Right Asymmetry in the Drell-Yan Process

This chapter goes over the analysis techniques and results from the 2015 transversely polarized Drell-Yan data taking. The chapter begins by describing the data collection setup and the event selection criteria followed by the analysis techniques used to determine asymmetry amplitudes. The analysis techniques described are the standard transverse spin-dependent amplitude (TSA) analysis, Sec 1.2, the double ratio analysis, Sec ??, the  $q_T$  weighted asymmetry analysis, Sec ??, and finally the left-right asymmetry analysis, Sec ??. All of these analyses are related in that they measure TMD effects from the Drell-Yan process. For this reason the event selection and kinematical asymmetry binning will all be the same unless noted otherwise.

### 1.1 Data Sample

The data sample is from the 2015 COMPASS Drell-Yan measurement where a 190 GeV/c  $\pi^-$  beam impinged on a transversely polarized  $\text{NH}_3$  target. The analysis data is from July 8, through November 12 which is after an initial spectrometer and beam commissioning phase. The data is split into 9 periods lasting approximated 2 weeks each, where each period consist of two sub-periods. To reduce systematic effects of acceptance and luminosity dependencies, the  $\text{NH}_3$  target was split into two oppositely polarized cells with one cell polarized vertically up and one cell polarized vertically down in the lab frame. The cells were separated by 20 cm and the polarization of both cells was flipped between sub-periods. A summary of the data taking from each period is shown in Table 1.1.

#### 1.1.1 Stability Tests

To ensure the data analyzed were recorded during stable beam and spectrometer conditions, stability of the analysis data was performed on a spill-by-spill and run-by-run basis. The data was recorded in runs with a maximum of 200 spills per run and where one spill can have several thousand events.

Period	Sub-period	Polarization	First-Last run	Begin date	End date
W07	one	↓↑	259363 - 259677	July 9	July 15
	two	↑↓	259744 - 260016	July 16	July 22
W08	one	↑↓	260074 - 260264	July 23	July 29
	two	↓↑	260317 - 260565	July 29	August 5
W09	one	↓↑	260627 - 260852	August 5	August 12
	two	↑↓	260895 - 261496	August 12	August 26
W10	one	↑↓	261515 - 261761	August 26	September 1
	two	↓↑	261970 - 262221	September 4	September 9
W11	one	↓↑	262370 - 262772	September 11	September 22
	two	↑↓	262831 - 263090	September 23	September 30
W12	one	↑↓	263143 - 263347	September 30	October 7
	two	↓↑	263386 - 263603	October 8	October 14
W13	one	↓↑	263655 - 263853	October 15	October 21
	two	↑↓	263926 - 264134	October 22	October 28
W14	one	↑↓	264170 - 264330	October 28	November 2
	two	↓↑	264429 - 264562	November 4	November 8
W15	one	↓↑	264619 - 264672	November 9	November 11
	two	↑↓	264736 - 264857	November 12	November 16

Table 1.1: COMPASS 2015 data taking periods

## Bad Spill Analysis

To determine if a given spill is deemed unstable several macro variables were averaged over the spill and compared to neighboring spills. These macro variables were chosen specifically to be sensitive to the general stability conditions of the spectrometer and are listed in the follower enumerated list Table 1.1.1. The starting criteria for an event was two oppositely charged muons where a muon was defined as having crossed 15 radiation lengths of material.

1. number of beam particles divided by the number of events
2. number of beam particles divided by the number of primary vertices
3. number of hits per beam track divided by the number of beam particles
4. number of primary vertices divided by the number of events
5. number of outgoing tracks divided by the number of events
6. number of outgoing particles from a primary vertex divided by the number of primary vertices
7. number of outgoing particle from primary vertex divided by the number of events
8. number of outgoing particles from primary vertex divided by the number of events
9. number of hits from outgoing particles divided by the number outgoing particles

10. number of  $\mu^+$  tracks divided by the number of events
11. number of  $\mu^+$  tracks from primary vertex divided by the number of events
12. number of  $\mu^-$  tracks divided by the number of events
13. number of  $\mu^-$  tracks from primary vertex divided by the number of events
14.  $\sum \chi^2$  of outgoing particles divided by the number of outgoing particles
15.  $\sum \chi^2$  of all vertices divided by the number of all vertices in an event
16. Trigger rates (LASxLAS, OTxLAS, LASxMT)

If the spectrometer was stable during a spill the average values from the variables in Table ?? are expected to be constant from one spill to the next. To determine if a spill was recorded in unstable conditions the spill of interest is compared with its neighboring 2500 spill occurring before and after in time. If the spill of interest is a specified sigma away from any of the neighboring spills too many times, the spill of interest is mark as a bad spill. If a spill fails this bad spill criteria for any of the macro variables in Table ?? the spill is deemed bad and not included in the analysis. The criteria for the sigma distance and number times a spill crosses this distance to be deemed a bad are different for each data taking period. In addition to checking the nearest spills for each spill, all the spills in a run are marked bad if the run it has less than 10 spills or greater than 70% bad spills. Table ?? describes to impact of the bad spill analysis on each period.

### Bad Run Analysis

The stability of the spectrometer is also verified on run-by-run check in parallel to the spill-by-spill check. The run-by-run analysis compares kinematic distributions and the average of these distributions per run to the same kinematic distributions and averages from the other runs in a given period. The kinematic distributions tested are:  $x_N$ ,  $x_\pi$ ,  $x_F$ ,  $q_T$ ,  $M_{\mu\mu}$ ,  $P_{\mu^+}$ ,  $P_{\mu^-}$ ,  $P_\gamma$ ,  $P_{\pi^-}$ , and vertex x, y and z positions. The quantities in the run-by-run analysis are expected to influence the asymmetries measured, however their distributions and averages are not expected to have spin-influenced effects from the limited statistics in just a single run. An unbinned-Kolmogorov test (UKT) is performed to compare each distributions. An UKT test is made between all the runs in a given period and a run is marked bad if it is incompatible with most of the runs in a period. The comparison of mean for each distribution from each run is made with the average from a given period. If one of the kinematical variables has an average more than five standard deviations from the average within a period, the run is rejected. The results of the bad spill rejection after having already applied the bad spill rejection are shown in Table ??.

Table 1.2: Stability analysis rejection percentages

Period	Bad spill rejection	Bad spill and spill rejection
W07	11.79%	17.94%
W08	18.00%	21.19%
W09	14.76%	17.11%
W10	15.88%	17.80%
W11	22.49%	26.14%
W12	12.71%	13.79%
W13	22.32%	22.73%
W14	8.91%	10.70%
W15	3.94%	3.94%

### 1.1.2 Event Selection

The cuts in the event selection were chosen to ensure the event consisted of two oppositely charged muons, so called dimuons, resulting from a pion collision in the transversely polarized target. The event selection was initial filtered from miniDSTs to  $\mu$ DSTs using the criteria of at least two muons detected in the spectrometer. The cuts used in this analysis are described in the following enumerated list where the event selection is performed on these  $\mu$ DSTs and the events used come from the slot1 production. A summary of the number of events remaining after the last cuts is shown in Table 1.1.

1. Two oppositely charged particles from a common best primary vertex. A primary vertex is defined as any vertex with an associated beam particle. In case of multiple common primary vertices the best primary vertex was determined by CORAL tagging the vertex as best primary (PHAST method `PaVertex::IsBestPrimary()`). In the case that CORAL did not tag any of the common vertices as the best primary the vertex with the smallest spatial  $\chi^2$  value was used as the best primary vertex.
2. A dimuon trigger fired. A dimuon trigger firing means there are at least two particles in coincidence in this event. The dimuon triggers used were a coincidence between two particles in the large angle spectrometer, LAS-LAS trigger, or a particle in the large angle spectrometer and a particle in the Outer hodoscope in the small angle spectrometer, LAS-Outer trigger. The LAS-Middle trigger was used as a veto on beam decay muons where beam decay muons result from the decay of the beam pion, kaon or anti-proton into a muon. This beam decay muon can then be in coincidence with a positive muon from another decay or strong reaction in the target. The LAS-Middle trigger was used a veto because this trigger was found to have many events resulting from a beam pion decaying to a muon.
3. Both particles are muons. A muon was defined as having crossed 30 radiation lengths of material between the particles first and last measured points. This criteria has been previously determined to

be effective at distinguishing between muons and hadrons. In the data production no detectors were used from upstream of the hadron absorber so the absorber is not included in the determination of material crossed.

4. The first measured point for both particles is before 300 cm and the last measured point is after 1500 cm. This cut ensures both particles have positions upstream of the first spectrometer magnet and downstream of the first muon filter.
5. The timing of both muons is defined. This checks that the time relative to the trigger time is determined for both muons so further timing cuts can be performed.
6. Both muons are in time within 5 nanoseconds. This track time for each muon is defined relative to the trigger time as in the previous cut. This cut helps rejected uncorrelated muons.
7. The muon track's spacial reduced  $\chi^2$ s are individually less than 10. This cut ensures track quality.
8. A validation that each muon crossed the trigger it was associated as having triggered. This trigger validation cut was performed by extrapolating (PHAST Method PaTrack::Extrapolate()) each muon track back to the hodoscopes it fired and determining if the muon crossed the geometric acceptance of both hodoscopes.
9. The event does not occur in the bad spill or run list. Many tests were performed to test the basic stability of the spectrometer and beam as described in section 1.1.1. The spills placed on the bad spill list were deemed to occur during unstable data taking conditions.
10. The Drell-Yan kinematics are physical. That is  $x_\pi$  and  $x_N$  are between 0 and 1 and  $x_F$  is between -1 and 1.
11. The transverse momentum of the virtual photon,  $q_T$  is between 0.4 and 5.0 GeV/c. The lower limit ensures azimuthal angular resolution is sufficient and the upper cut is minimal and further ensures the kinematic distributions are physically possible.
12. The vertex originated within the z-positions of the transversely polarized target cells defined by the target group ( $-294.5 < Z_{\text{vertex}} < -239.3$  for the upstream target or  $-219.5 < Z_{\text{vertex}} < -164.3$  cm for the downstream target).
13. The vertex is within the radius of the polarized target measured to be 1.9 cm.

Cuts	W07	W08	W09	W10	W11	W12	W13	W14	W15	W16	% Remaining
All Data	19410	19184	19654	20707	31371	23563	20561	13154	7697	175301	100.00 %
Good Spills	15947	14899	16217	16895	23041	20184	16026	11796	7422	142427	81.70 %
$0 < x_\pi \ x_N < 1, -1 < x_F < 1$	15932	14886	16200	16885	23022	20171	16013	11794	7414	142317	81.70 %
$0.4 < q_T < 5(\text{GeV}/c)$	14342	13385	14609	15239	20667	18101	14365	10588	6636	127932	60.75 %
Z Vertex within $\text{NH}_3$	4256	4024	4330	4552	6369	5503	4411	3130	2028	38603	15.05 %
Vertex Radius $< 1.9\text{cm}$	4175	3950	4257	4474	6252	5414	4334	3078	1987	37921	12.21 %

Figure 1.1: Event selection statistics for this analysis

### 1.1.3 Binning

The asymmetries are measured in bins of  $x_N$ ,  $x_\pi$ ,  $x_F$ ,  $q_T$ , and  $M_{\mu\mu}$ . Where  $x_N$  and  $x_\pi$  the momentum fractions of the target nucleon and beam pion respectively,  $x_F = x_\pi - x_N$ ,  $q_T$  is the transverse momentum of the virtual photon and  $M_{\mu\mu}$  is the invariant mass of the di-muon. The binning was determined by requiring equal statistical population in each kinematic bin. In addition, the asymmetries are determined in an integrated bin using all the analysis data. The analyzes binning limits are summarized in Table 1.3.

Kinematics	Lowest limit	Upper limit bin 1	Upper limit bin 2	Upper limit bin 3
$x_N$	0.0	0.13	0.19	1.0
$x_\pi$	0.0	0.40	0.56	1.0
$x_F$	-1.0	0.22	0.41	1.0
$q_T$ (GeV/c)	0.4	0.86	1.36	5.0
$M_{\mu\mu}$ (GeV/c <sup>2</sup> )	4.3	4.73	5.50	8.5

Table 1.3: Analysis binning limits

## 1.2 Transverse Spin-Dependent Asymmetries

This section describes the standard TSA analysis for which the results are published in reference [1]. The main motivation for this analysis was to measure the sign of the Sivers function flip between Drell-Yan and SIDIS using data from the same experimental setup for both processes.

As was noted in the event selection 1.1.2, the data considered are in the invariant mass range [4.3-8.5 GeV/c<sup>2</sup>]. Fig. 1.2 shows the invariant mass range from the 2015 COMPASS data with all cuts except the invariant mass range cut along with a fit to show the background processes. The fit is determined by Monte-Carlo data and combinatorial background analysis. The Monte-Carlo data simulated all hard processes which decay to two oppositely charged muons and can be reconstructed in the COMPASS spectrometer. Combinatorial background analysis estimates the background as  $N_{combinatorial} = 2\sqrt{N_{\mu^+\mu^-} + N_{\mu^-\mu^+}}$ . As can be seen there are two background peaks. The lower mass peak at about 3 GeV/c<sup>2</sup> corresponds to J/Ψ production and the mass peak at around 3.6 GeV/c<sup>2</sup> corresponds to Ψ' production. As can be seen, in

the mass range for all the analyses in this chapter,  $[4.3\text{-}8.5 \text{ GeV}/c^2]$ , the Drell-Yan process dominates. The background percentage was estimated to be below 4% in this analysis mass range.

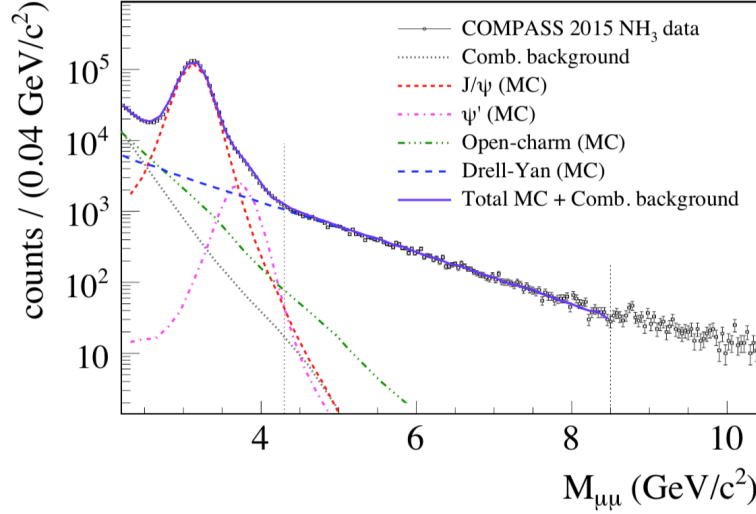
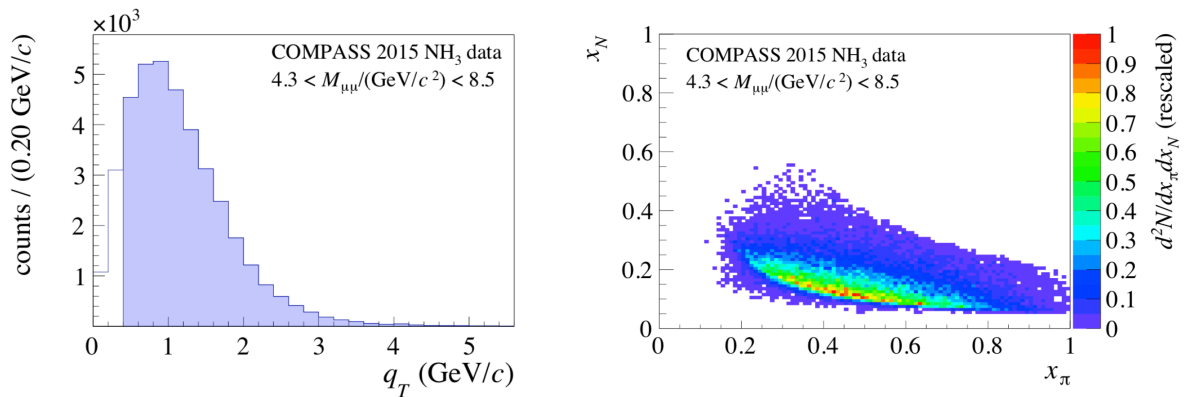


Figure 1.2: The 2015 COMPASS invariant dimuon mass distribution and data fit. The data fit is from Monte-Carlo and combinatorial background analysis and is provided to show the background processes. This image is taken from [1].

Fig. 1.3a shows the transverse virtual photon momentum,  $q_T$ , distribution for this analysis. The average  $q_T$  for these analyses is  $1.2 \text{ GeV}/c$  while the average  $M_{\mu\mu}$  is  $5.3 \text{ GeV}/c^2$ . As stated in chapter ??, the regime where TMD functions are the theoretical model for parton distributions is when  $q_T \ll M_{\mu\mu}$ . While the average  $q_T$  is less than the average  $M_{\mu\mu}$ , it is not excluded that the results in this chapter are outside of the TMD limit. Nevertheless the result present are determined assuming the analyses are performed in the TMD regime.



(a) The  $q_T$  distribution where the shaded regions shows the data used in the high mass analysis and the unshaded region shows the full distribution without a  $q_T$  cut. This image is taken from [1].

(b) The 2-dimensional distribution of  $x_\pi$  vs.  $x_N$ . Both  $x_\pi$  and  $x_N$  are safely in their respective valence regions. This image is taken from [1].

The distribution of  $x_\pi$  versus  $x_N$  is shown in Fig. 1.3b. The Bjorken- $x$  of the proton,  $x_N$ , is almost exclusively above 0.1 and as well Bjorken- $x$  for the pion,  $x_\pi$  is in its valence region. For these reasons it is safe to say that the Drell-Yan reaction studied these analyses is the result of the pion's anti-u-quark annihilating with the proton's u-quark.

The results in this section are determined from an extended unbinned maximum likelihood fit to the data. The dilution and depolarization values are determined on an event by event basis unlike the other analyses in this chapter. The released integrated results for the leading order and sub-leading order TSAs are shown in Fig. 1.4. The leading order TSAs are non-zero with approximate significances of: 1 sigma for  $A_T^{\sin(\phi_S)}$ , 1.2 sigma for  $A_T^{\sin(2\phi_{CS}+\phi_S)}$  and 2 sigma for  $A_T^{\sin(2\phi_{CS}-\phi_S)}$ .

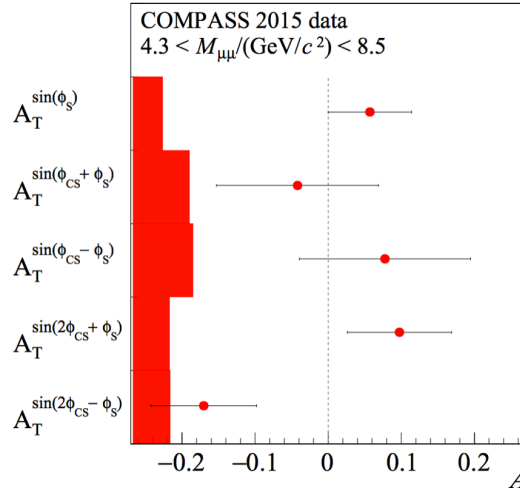


Figure 1.4: The integrated TSAs with statistical and systematic error bars.  $A_T^{\sin(\phi_S)}$ ,  $A_T^{\sin(2\phi_{CS}+\phi_S)}$ , and  $A_T^{\sin(2\phi_{CS}-\phi_S)}$  are leading order TSAs and  $A_T^{\sin(\phi_{CS}+\phi_S)}$  and  $A_T^{\sin(\phi_{CS}-\phi_S)}$  are sub-leading order TSAs.

The comparison of the Sivers TSA,  $A_T^{\sin(\phi_S)}$ , with the expected sign flip is shown in Fig. 1.5. The positive solid theory curves show the expected Sivers TSA assuming the Sivers function flips sign between Drell-Yan and SIDIS. The main difference in these three theory curves is the  $Q^2$  evolution technique used. As can be seen the Sivers TSA is compatible with the expected sign change. However, the error bars on the Sivers asymmetry amplitude are too large to conclusively distinguish between the three theory curves or even to conclusively conclude on the sign change between Drell-Yan and SIDIS. That being said, the amplitude  $A_T^{\sin(\phi_S)}$  is 2 sigma away from being incompatible with the sign flip.



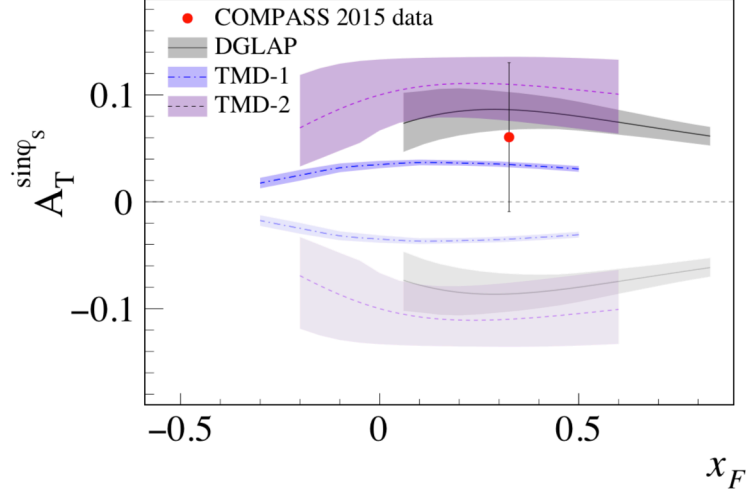


Figure 1.5: The Siverts TSA along with theory curves for the expected sign change (solid curves) and without the sign change (opaque curves). Theory curves and uncertainties are calculated using  $Q^2$  evolution from DGLAP [2], TMD-1 [3], TMD-2 [4]. This image is taken from [1].

### 1.3 Extraction of Left-Right Asymmetries

This section goes over the analysis details for measuring the left-right asymmetry from transversely polarized Drell-Yan data. A theoretical introduction showing how the left-right asymmetry is related to TMD PDFs and related past result for this asymmetry are given in Sec ???. In short the measured asymmetry can be defined as

$$A_{lr} = \frac{\sigma_{Left} - \sigma_{Right}}{\sigma_{Left} + \sigma_{Right}}. \quad (1.1)$$

There are many ways to determine the left-right asymmetry denoted as  $A_N$ . The relevant techniques for the 2015 COMPASS setup are described and compared to ensure confidence in the end results. Sec. 1.3.1 starts with a general introduction to the notations and ideas used for all the asymmetry methods.

#### 1.3.1 Geometric Mean

The number of physics counts,  $N$ , detected from any particular target can be written as

$$N = L * \sigma * a, \quad (1.2)$$

where  $L$  is the luminosity,  $\sigma$  is the cross-section of such an event and  $a$  is the acceptance. In this formula the acceptance is a function of detector efficiencies and the spectrometer acceptance. In simple words, the number of counts detected is the number of possible chances for an event to occur times the probability for an event to occur and that the event will be detected. To get spin-dependent counts for the left-right

asymmetry, the target, polarization and left or right direction relative to the spin have to be included in the counts. Generically this can be written

$$N_{\text{cell,L(R)}}^{\uparrow(\downarrow)} = a_{\text{cell,spectrometer direction}}^{\uparrow(\downarrow)} * L_{\text{cell}}^{\uparrow(\downarrow)} * \sigma_{\text{L(R)}}, \quad (1.3)$$

where  $\uparrow(\downarrow)$  denotes the target polarization, cell is either cell 1 for the upstream target cell or cell 2 for the downstream target cell, L(R) is left(right) of the spin direction and spectrometer direction denotes either the spectrometer Jura side or the Saleve side corresponding to where the event was detected.

The most basic method to determine  $A_N$  per target cell is

$$A_N = \frac{1}{P} \frac{N_L - N_R}{N_L + N_R}, \quad (1.4)$$

where the counts,  $N$ , are defined as Eq. 1.2, and  $P$  denotes the fraction of polarized nucleons. An intuitive picture of left and right defined in the target frame is shown in Fig. 1.6.

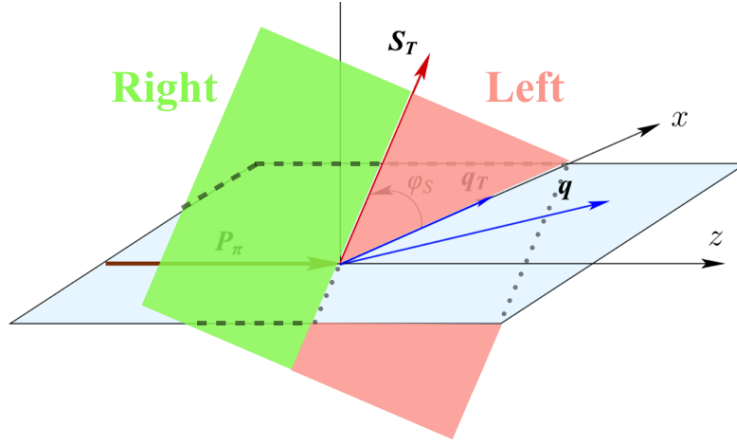


Figure 1.6: The definition of the left plane (red) and right plane (green) defined from a target spin up configuration in the target frame

The previous definitions of the detected counts, Eq. 1.3 and Eq. 1.2, and therefore also Eq. 1.4 all depend on the spectrometer acceptance. This is a problem because the spectrometer acceptance can change with time and space and therefore can be dependent on the physical kinematics which produced the event. Such dependencies can cause unphysical false asymmetries in the measurement of  $A_N$  and must therefore be removed or must be included as systematic effects.

Forming the geometric mean asymmetry is, however, a way to determine the left-right asymmetry without

acceptance effects from the spectrometer. It is defined as

$$\frac{1}{P} \frac{\sqrt{N_{\text{cell } 1(2),L}^{\uparrow} N_{\text{cell } 1(2),L}^{\downarrow}} - \sqrt{N_{\text{cell } 1(2),R}^{\uparrow} N_{\text{cell } 1(2),R}^{\downarrow}}}{\sqrt{N_{\text{cell } 1(2),L}^{\uparrow} N_{\text{cell } 1(2),L}^{\downarrow}} + \sqrt{N_{\text{cell } 1(2),R}^{\uparrow} N_{\text{cell } 1(2),R}^{\downarrow}}}, \quad (1.5)$$

where P represents the fraction of polarized nucleons. Table ?? summarizes the notations used throughout this chapter.

Table 1.4: Notations used in defining the left/right asymmetry

Notation	Description
L(R)	virtual photon detected left(right) of spin
Jura(Saleve)	spectrometer west(east) side
cell 1(2)	up(down)stream target cell
$\uparrow(\downarrow)$	target cell polarized up(down)
P	fraction of polarized target nucleons

Equation 1.5 can be thought of simply as the normalized difference of left minus right counts. Left and right counts are determined relative to the target spin directions and are defined as

$$\begin{aligned} \text{Left} : \hat{q}_T \cdot (\hat{S}_T \times \hat{P}_\pi) &> 0 \\ \text{Right} : \hat{q}_T \cdot (\hat{S}_T \times \hat{P}_\pi) &< 0, \end{aligned} \quad (1.6)$$

where  $\hat{q}_T$ ,  $\hat{S}_T$  and  $\hat{P}_\pi$  are unit vectors in the target reference frame for the virtual photon transverse momentum, the target spin and the beam pion momentum respectively.

Using Eq. 1.3 for the definition of counts, the geometric mean asymmetry is

$$\frac{1}{P} \frac{\kappa_{\text{geomean}} \sqrt{\sigma_L \sigma_L} - \sqrt{\sigma_R \sigma_R}}{\kappa_{\text{geomean}} \sqrt{\sigma_L \sigma_L} + \sqrt{\sigma_R \sigma_R}}, \quad (1.7)$$

where  $\kappa$  is a ratio of acceptances defined as

$$\kappa_{\text{geomean}} = \frac{\sqrt{a_{\text{cell } 1(2),\text{Jura}}^{\uparrow} a_{\text{cell } 1(2),\text{Saleve}}^{\downarrow}}}{\sqrt{a_{\text{cell } 1(2),\text{Saleve}}^{\uparrow} a_{\text{cell } 1(2),\text{Jura}}^{\downarrow}}}. \quad (1.8)$$

Here the detection side of spectrometer is specified by looking down the beam line as either Jura to mean left or Saleve to mean right. These relations of Jura is left and Saleve is right are only strictly true if the target polarization is pointing straight up in the target frame. In particular if the beam particle and the target polarization do not make a right angle in the laboratory frame this relation will no longer be strictly true but is an approximation for ease of notation.

Relation 1.7 is equal to  $A_N$  if  $\kappa$  is equal to one. However as stated previously, time effects can vary  $\kappa$  from unity. These effects are estimated through false asymmetry analysis and included in the systematic error bars described in section 1.4. Equation 1.5 is therefore to a good approximation an acceptance free method to determine  $A_N$ . It is also defined for the upstream and downstream cells independently and therefore can be used as a consistency check between the two target cells.

The statistical uncertainty of the geometry mean is

$$\frac{1}{P} \frac{\sqrt{N_L^\uparrow N_L^\downarrow N_R^\uparrow N_R^\downarrow}}{\left(\sqrt{N_L^\uparrow N_L^\downarrow} + \sqrt{N_R^\uparrow N_R^\downarrow}\right)^2} \sqrt{\frac{1}{N_L^\uparrow} + \frac{1}{N_L^\downarrow} + \frac{1}{N_R^\uparrow} + \frac{1}{N_R^\downarrow}}, \quad (1.9)$$

which reduces to  $\frac{1}{P} \frac{1}{\sqrt{N}}$  in the case of equal statistics in each direction from each target cell polarization.

### 1.3.2 Two-Target Geometric Mean

As described in section 1.1 COMPASS had two oppositely polarized target cells in 2015. The previous geometric mean asymmetry, however, determined an  $A_N$  per target. It is desirable from a statistical point of view, however, to determine one  $A_N$  from the 2015 COMPASS setup. It is also desirable for comparison purposes to determine  $A_N$  using all the information from the 2015 COMPASS setup. This can be accomplished by modifying the geometric mean to add both target cells as follows

$$\frac{1}{P} \frac{\sqrt[4]{N_{\text{cell } 1, L}^\uparrow N_{\text{cell } 1, L}^\downarrow N_{\text{cell } 2, L}^\uparrow N_{\text{cell } 2, L}^\downarrow} - \sqrt[4]{N_{\text{cell } 1, R}^\uparrow N_{\text{cell } 1, R}^\downarrow N_{\text{cell } 2, R}^\uparrow N_{\text{cell } 2, R}^\downarrow}}{\sqrt[4]{N_{\text{cell } 1, L}^\uparrow N_{\text{cell } 1, L}^\downarrow N_{\text{cell } 2, L}^\uparrow N_{\text{cell } 2, L}^\downarrow} + \sqrt[4]{N_{\text{cell } 1, R}^\uparrow N_{\text{cell } 1, R}^\downarrow N_{\text{cell } 2, R}^\uparrow N_{\text{cell } 2, R}^\downarrow}}. \quad (1.10)$$

As in the basic geometric mean asymmetry, section 1.3.1, left and right are determined relative to the spin direction of the target as in Eq. 1.6. Again using Eq. 1.3 for the definition of counts, the two target geometric mean asymmetry, Eq. 1.10, can be written as

$$\frac{1}{P} \frac{\kappa_{\text{two-target}} \sqrt[4]{\sigma_L \sigma_L \sigma_L \sigma_L} - \sqrt[4]{\sigma_R \sigma_R \sigma_R \sigma_R}}{\kappa_{\text{two-target}} \sqrt[4]{\sigma_L \sigma_L \sigma_L \sigma_L} + \sqrt[4]{\sigma_R \sigma_R \sigma_R \sigma_R}}, \quad (1.11)$$

,

where now  $\kappa_{\text{two-target}}$  is the ratio of acceptances from all targets and polarizations. This inclusive acceptance ratio is defined as

$$\kappa_{\text{two-target}} = \frac{\sqrt[4]{a_{\text{cell } 1, \text{Jura}}^\uparrow a_{\text{cell } 1, \text{Saleve}}^\downarrow a_{\text{cell } 2, \text{Jura}}^\uparrow a_{\text{cell } 2, \text{Saleve}}^\downarrow}}{\sqrt[4]{a_{\text{cell } 1, \text{Saleve}}^\uparrow a_{\text{cell } 1, \text{Jura}}^\downarrow a_{\text{cell } 2, \text{Saleve}}^\uparrow a_{\text{cell } 2, \text{Jura}}^\downarrow}}. \quad (1.12)$$

In this case the acceptance ratio is expected to vary less with time and therefore be closer to unity than

the normal geometric mean acceptance ratio, Eq. 1.8. This is a consequence of having the different target cells oppositely polarized. Rewriting Eq. 1.12 with sub-period superscripts instead of target polarization superscripts

$$\kappa_{two-target} = \frac{\sqrt[4]{a_{\text{cell } 1, \text{Jura}}^a a_{\text{cell } 1, \text{Saleve}}^b a_{\text{cell } 2, \text{Jura}}^b a_{\text{cell } 2, \text{Saleve}}^a}}{\sqrt[4]{a_{\text{cell } 1, \text{Saleve}}^a a_{\text{cell } 1, \text{Jura}}^b a_{\text{cell } 2, \text{Saleve}}^b a_{\text{cell } 2, \text{Jura}}^a}}, \quad (1.13)$$

where sub-period  $a$  is with the upstream target polarized up and the downstream target polarized down and vice versa for sub-period  $b$ . From Eq. 1.13 it is more evident that the acceptance ratio terms for sub-period  $b$  are reciprocal to the terms for sub-period  $a$  and therefore the acceptance ratio is expected to be more stably close to unity.

Finally the statistical uncertainty of the two target geometric mean is

$$\frac{1}{P} \frac{LR}{(L+R)^2} \sqrt{\sum_{\text{cell}} \sum_{\text{polarization}} \left( \frac{1}{N_{\text{cell},L}^{\text{polarization}}} + \frac{1}{N_{\text{cell},R}^{\text{polarization}}} \right)}, \quad (1.14)$$

where L can be thought of as the left counts and equals to  $\sqrt[4]{N_{\text{cell } 1, L}^{\uparrow} N_{\text{cell } 1, L}^{\downarrow} N_{\text{cell } 2, L}^{\uparrow} N_{\text{cell } 2, L}^{\downarrow}}$  and R can be thought of as the right counts and equals  $\sqrt[4]{N_{\text{cell } 1, R}^{\uparrow} N_{\text{cell } 1, R}^{\downarrow} N_{\text{cell } 2, R}^{\uparrow} N_{\text{cell } 2, R}^{\downarrow}}$ . The statistical uncertainty for the two target geometric mean also reduces to  $\frac{1}{P} \frac{1}{\sqrt{N}}$  in the case of equal statistic populations in each direction and target polarization.

## 1.4 Systematic Studies

Several tests were performed to estimate the systematic uncertainty of the left-right asymmetry. The systematic errors are determined by adding all non-zero systematic uncertainties in quadrature. The impact from each source of systematic error is summarized in Tab. 1.7.

### 1.4.1 Period Compatibility (Time Dependence)

The asymmetries calculated for each time period in each kinematic bin are shown in Fig. 1.7.

By eye the asymmetry fluctuations appear to be statistically compatible. To quantify the compatibility of the asymmetries between the periods, a pull distribution is formed. The pull value is defined as

$$\Delta A_i = \frac{A_i - \langle A \rangle}{\sqrt{\sigma_{A_i}^2 - \sigma_{\langle A \rangle}^2}}, \quad (1.15)$$

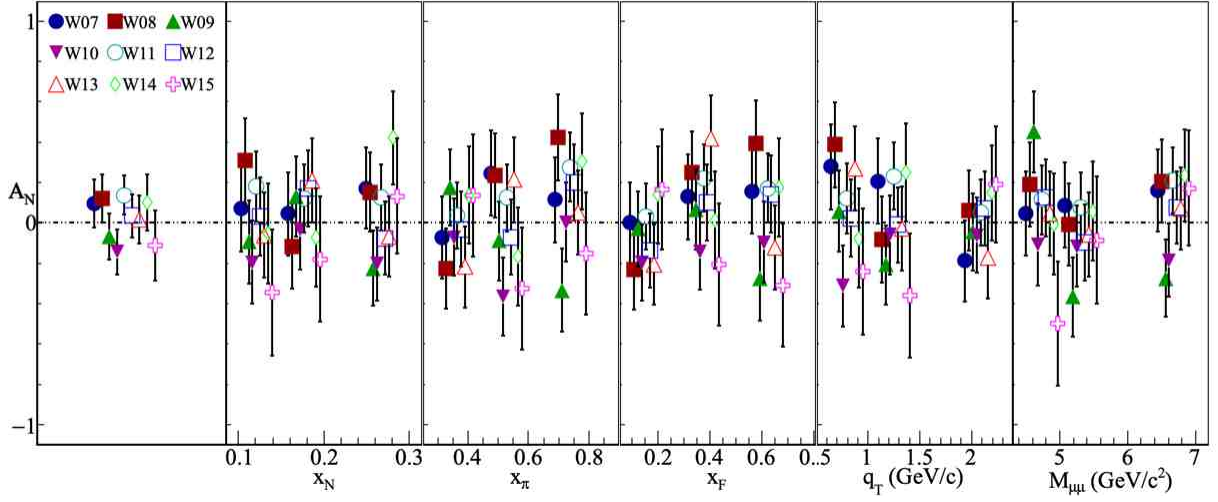


Figure 1.7:  $A_N$  determined for each period

and is determined for each period and kinematic bin. There are therefore 3 (number of bins)  $\times$  5 (number of kinematics)  $\times$  9 (number of periods) = 135 entries in the pull distribution. This distribution is shown in Fig. 1.8 along with a Gaussian fit. If the asymmetries all come from the same parent distribution then due to the central limit theorem the pull distribution will be a Gaussian distribution with zero mean and unit variance. The discrepancy of the pull distribution from a standard Gaussian distribution is used to determine a systematic error as

$$\frac{\sigma_{\text{systematic}}}{\sigma_{\text{statistical}}} = \sqrt{|\sigma_{\text{pull}}^2 - 1| + \frac{\mu_{\text{pull}}^2}{2}}. \quad (1.16)$$

As the asymmetries in different kinematic bins are formed using the same data set the asymmetries between kinematic binning are correlated. For this reason an uncorrelated pull distribution is also formed for each kinematic bin and also compared with a standard Gaussian distribution. These distributions are shown in Fig. 1.9 and the results of the Gaussian fit are shown in Fig. 1.10. For these uncorrelated pull distributions there are now only 3 (number of bins)  $\times$  9 (number of periods) = 27 entries in each kinetically binned pull distributions and only 9 (number of periods) bins in the integrated pull distribution.

Even though the Gaussian fits did not give exactly a standard Gaussian, the fit parameters are well compatible with a standard Gaussian within the errors of the fit. Therefore no systematic error was assigned due to incompatibility of the periods.

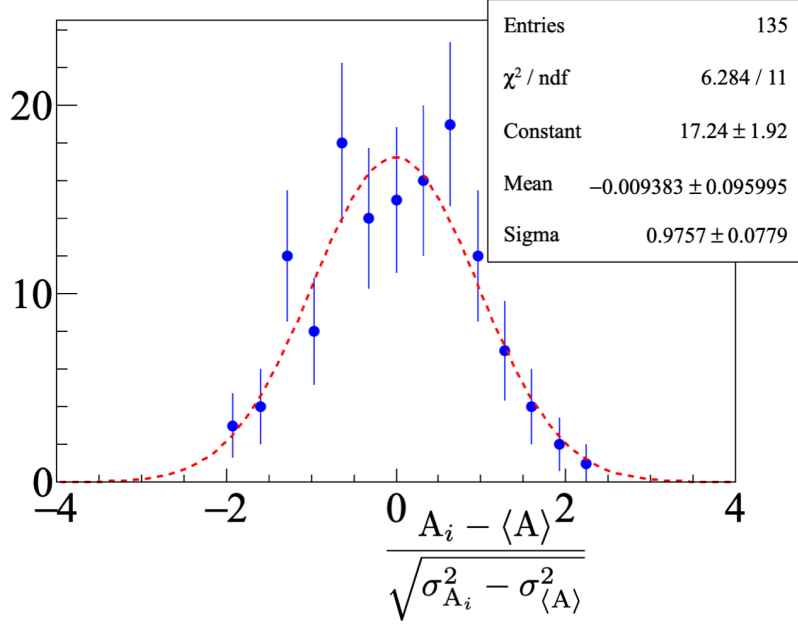


Figure 1.8: Pull distribution from the two target geometric mean

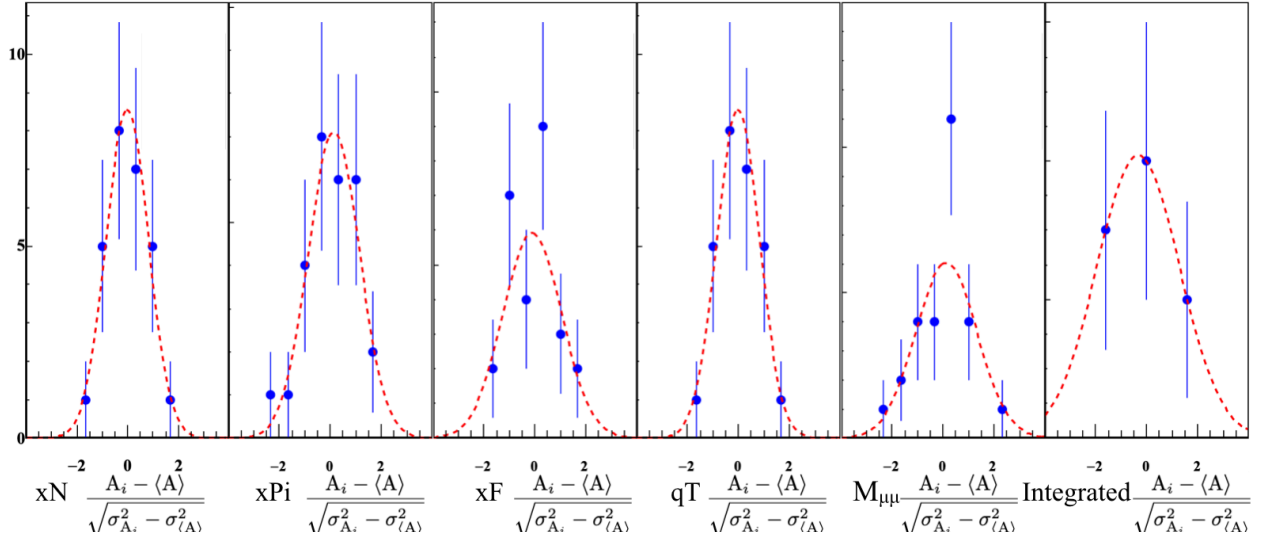


Figure 1.9: Uncorrelated pull distributions

Entries	27	Entries	27	Entries	27	Entries	27	Entries	27	Entries	9
$\chi^2 / \text{ndf}$	0.4347 / 3	$\chi^2 / \text{ndf}$	1.056 / 4	$\chi^2 / \text{ndf}$	3.416 / 3	$\chi^2 / \text{ndf}$	0.4347 / 3	$\chi^2 / \text{ndf}$	3.152 / 4	$\chi^2 / \text{ndf}$	1.091e-08 / 0
Constant	$8.548 \pm 2.043$	Constant	$7.101 \pm 1.827$	Constant	$5.922 \pm 1.622$	Constant	$8.548 \pm 2.043$	Constant	$6.038 \pm 1.603$	Constant	$4.085 \pm 1.992$
Mean	$-0.01562 \pm 0.17221$	Mean	$0.1422 \pm 0.2204$	Mean	$-0.1036 \pm 0.2910$	Mean	$-0.01562 \pm 0.17221$	Mean	$0.1287 \pm 0.2860$	Mean	$-0.3308 \pm 0.8192$
Sigma	$0.8386 \pm 0.1304$	Sigma	$1.004 \pm 0.201$	Sigma	$1.15 \pm 0.31$	Sigma	$0.8386 \pm 0.1304$	Sigma	$1.197 \pm 0.256$	Sigma	$1.616 \pm 1.101$

Figure 1.10: Results of Gaussian fit for the uncorrelated pull distributions

## 1.4.2 False Asymmetries

### Acceptance From False Asymmetries

As was pointed out in Sec. 1.3.1 and Sec. 1.3.2, the asymmetry measurement assumes the acceptance does not change with time and therefore the acceptance ratios Eq. 1.8 and Eq. 1.12 are unitary. Any deviation from a unitary acceptance ratio is estimated with a false asymmetry and is taken as a systematic error. To determine if acceptance does change with time, a false asymmetry is calculated where the only way the false asymmetry could be non-zero is if acceptance changes with time. This false asymmetry for the two target geometric mean is

$$\begin{aligned}
A_{N,\text{False}} &= \frac{1}{P} \frac{\sqrt[4]{N_{\text{cell } 1, \text{R}}^{\uparrow} N_{\text{cell } 1, \text{L}}^{\downarrow} N_{\text{cell } 2, \text{L}}^{\uparrow} N_{\text{cell } 2, \text{R}}^{\downarrow}} - \sqrt[4]{N_{\text{cell } 1, \text{L}}^{\uparrow} N_{\text{cell } 1, \text{R}}^{\downarrow} N_{\text{cell } 2, \text{R}}^{\uparrow} N_{\text{cell } 2, \text{L}}^{\downarrow}}}{\sqrt[4]{N_{\text{cell } 1, \text{R}}^{\uparrow} N_{\text{cell } 1, \text{L}}^{\downarrow} N_{\text{cell } 2, \text{L}}^{\uparrow} N_{\text{cell } 2, \text{R}}^{\downarrow}} + \sqrt[4]{N_{\text{cell } 1, \text{L}}^{\uparrow} N_{\text{cell } 1, \text{R}}^{\downarrow} N_{\text{cell } 2, \text{R}}^{\uparrow} N_{\text{cell } 2, \text{L}}^{\downarrow}}} \\
&= \frac{1}{P} \frac{\alpha \sqrt[4]{\sigma_R \sigma_L \sigma_L \sigma_R} - \sqrt[4]{\sigma_L \sigma_R \sigma_R \sigma_L}}{\alpha \sqrt[4]{\sigma_R \sigma_L \sigma_L \sigma_R} + \sqrt[4]{\sigma_L \sigma_R \sigma_R \sigma_L}}
\end{aligned} \tag{1.17}$$

$$= \frac{1}{P} \frac{\alpha - 1}{\alpha + 1}, \tag{1.18}$$

where  $\alpha$  is an acceptance ratio and is defined as

$$\alpha = \frac{\sqrt[4]{a_{\text{cell } 1, \text{Saleve}}^{\uparrow} a_{\text{cell } 1, \text{Saleve}}^{\downarrow} a_{\text{cell } 2, \text{Jura}}^{\uparrow} a_{\text{cell } 2, \text{Jura}}^{\downarrow}}}{\sqrt[4]{a_{\text{cell } 1, \text{Jura}}^{\uparrow} a_{\text{cell } 1, \text{Jura}}^{\downarrow} a_{\text{cell } 2, \text{Saleve}}^{\uparrow} a_{\text{cell } 2, \text{Saleve}}^{\downarrow}}}. \tag{1.19}$$



The false asymmetry, Eq. 1.17, can be simplified as

$$A_{N,\text{False}} = \frac{1}{P} \frac{\sqrt[4]{N_{\text{cell 1,Saleve}} N_{\text{cell 2,Jura}}} - \sqrt[4]{N_{\text{cell 1,Jura}} N_{\text{cell 2,Saleve}}}}{\sqrt[4]{N_{\text{cell 1,Saleve}} N_{\text{cell 2,Jura}}} + \sqrt[4]{N_{\text{cell 1,Jura}} N_{\text{cell 2,Saleve}}}}. \quad (1.20)$$

That is  $A_{N,\text{false}}$  is the normalized difference of counts from each target cell assuming the upstream target is always polarized down and the downstream target is always polarized up. Given that the polarization flips for both upstream and downstream target cells,  $A_{N,\text{false}}$  is an asymmetry where physical effects cancel out. The kinematic dependencies of the false asymmetry are shown in Fig. 1.11 and the kinematic dependencies of the acceptance ratio,  $\alpha$ , are shown in Fig. 1.12.

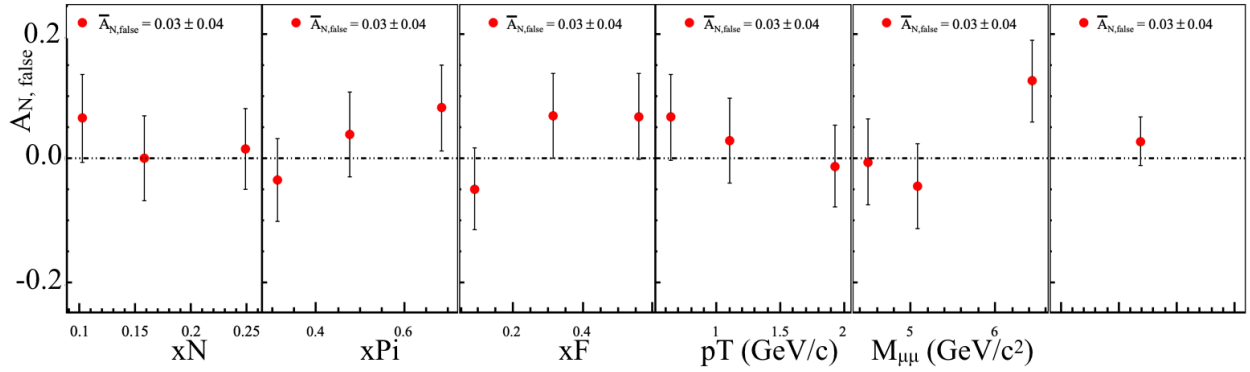


Figure 1.11: False asymmetry to estimate fluctuations in acceptance in time

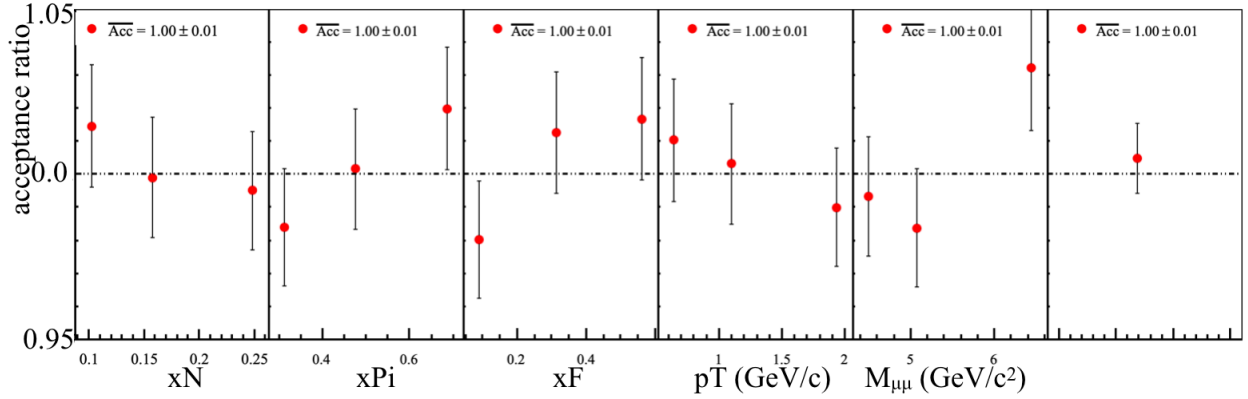


Figure 1.12: Acceptance ratio, Eq. 1.19, used to determine the systematic effects from acceptance changes in time

While  $\alpha$  is an acceptance ratio it is not the same as the acceptance ratio in the true asymmetry. However  $\alpha$  is similar to the true acceptance ratio,  $\kappa$ , in that  $\alpha$  will only be different from unity as a result of time changes in the spectrometer. Therefore it is assumed  $\alpha$  can be used as a good estimate of the true acceptance

ratio fluctuations. The systematic error due to acceptance fluctuations is determined as

$$\delta A_{N,\text{systematic}} = \frac{1}{P} \left( \frac{|\alpha - 1|}{2} + \delta_{\frac{|\alpha-1|}{2}} \right), \quad (1.21)$$

where this expression is derived in Appendix ???. The kinematic dependence of the systematic error normalized to the statistical error is shown in Fig. 1.13. The binned average systematic error due to acceptance is 20% of the statistical error.

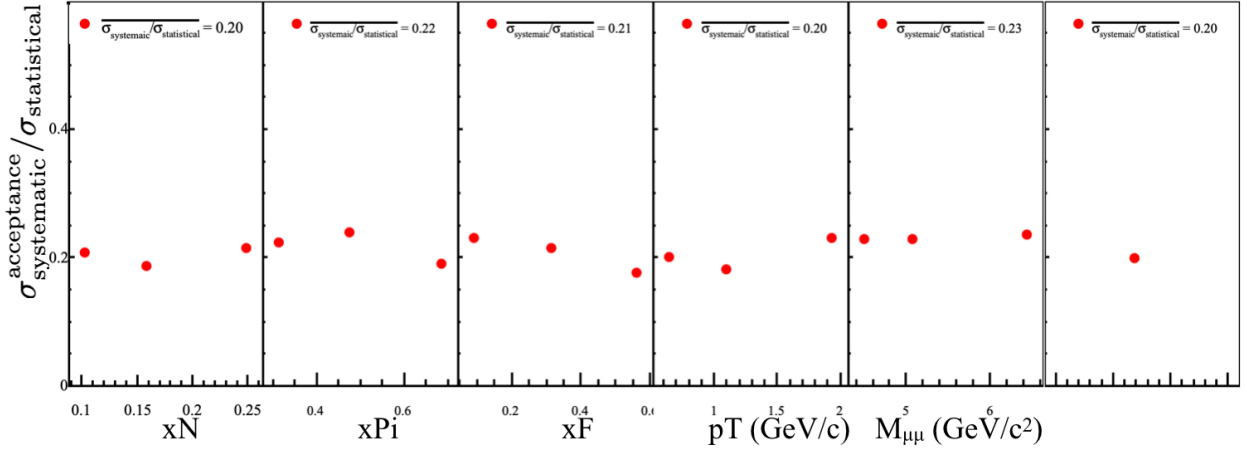


Figure 1.13: Systematic error due to acceptance effects

### 1.4.3 Further False Asymmetry Effects

Although the list of systematic effects specifically studied is quite exhaustive there is always the potential for other systematic effects not considered. Studies of the changes in time from additional false asymmetries were performed in an attempt to taken into account all other systematic effects. All false asymmetries considered must be constructed in such a way that the physical process of interest cancels out. A false asymmetry could therefore only be non-zero from acceptance effects, luminosity or some other reason not considered. The additional false asymmetries are constructed in a way that luminosity effects cancel out and acceptance effects are approximately constant. With these assumptions, the pull values from Eq. 1.15 are expected to be distributed as a standard Gaussian distribution. Any deviation from a standard Gaussian is conservatively taken as a systematic effect from some unknown cause. The additional studied false asymmetries are summarized in the following enumerated list.

1. A false asymmetry similar to Eq. 1.17 but with the upstream left and right counts flipped defined as

$$\frac{1}{P} \frac{\sqrt[4]{N_{\text{cell } 1, L}^{\uparrow} N_{\text{cell } 1, R}^{\downarrow} N_{\text{cell } 2, L}^{\uparrow} N_{\text{cell } 2, R}^{\downarrow}} - \sqrt[4]{N_{\text{cell } 1, R}^{\uparrow} N_{\text{cell } 1, L}^{\downarrow} N_{\text{cell } 2, R}^{\uparrow} N_{\text{cell } 2, L}^{\downarrow}}}{\sqrt[4]{N_{\text{cell } 1, L}^{\uparrow} N_{\text{cell } 1, R}^{\downarrow} N_{\text{cell } 2, L}^{\uparrow} N_{\text{cell } 2, R}^{\downarrow}} + \sqrt[4]{N_{\text{cell } 1, R}^{\uparrow} N_{\text{cell } 1, L}^{\downarrow} N_{\text{cell } 2, R}^{\uparrow} N_{\text{cell } 2, L}^{\downarrow}}}. \quad (1.22)$$

This false asymmetry can be thought of as measuring the normalized counts on the Jura side minus the Saleve side. The period weighted average results of this false asymmetry are shown in Fig. 1.14 and as can be seen there is the asymmetry is systematically less than zero by more than a standard deviation. The uncorrelated pull distributions from this false asymmetry are shown in Fig. 1.15 and the corresponding Gaussian fit results are shown in Fig. 1.16. Due to the fact that there are less entries in these pull distributions the Gaussian fit results are not necessarily that good. In an attempt to correct for this and to take into account the fit errors, a weighted average of the mean and standard deviation are made, as in Eq. 1.26, using weights as the inverse fit variances. The resulting systematic error is again determined as in Eq. 1.16 using the weighted mean and weighted standard deviation.

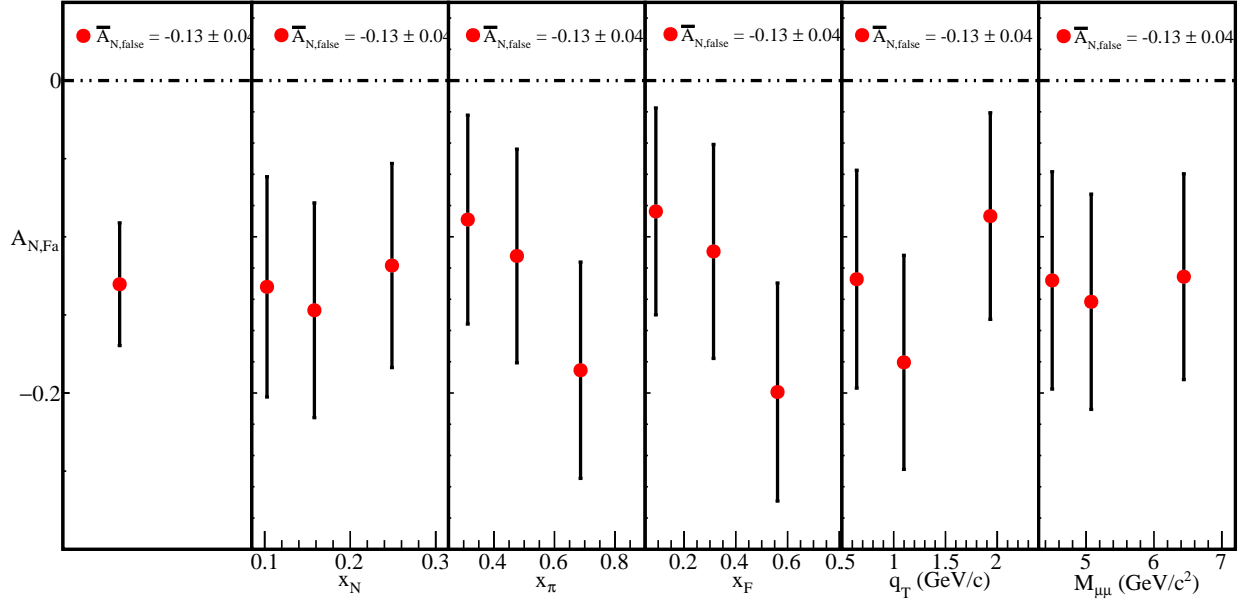


Figure 1.14: Two target geomean false asymmetry. This is non-zero due to acceptance effects

2. A false asymmetries using only the information from the upstream or the downstream target defined as

$$\frac{1}{P} \frac{\sqrt{N_{\text{cell } 1(2), L}^{\uparrow} N_{\text{cell } 1(2), R}^{\downarrow}} - \sqrt{N_{\text{cell } 1(2), R}^{\uparrow} N_{\text{cell } 1(2), L}^{\downarrow}}}{\sqrt{N_{\text{cell } 1(2), L}^{\uparrow} N_{\text{cell } 1(2), R}^{\downarrow}} + \sqrt{N_{\text{cell } 1(2), R}^{\uparrow} N_{\text{cell } 1(2), L}^{\downarrow}}}. \quad (1.23)$$

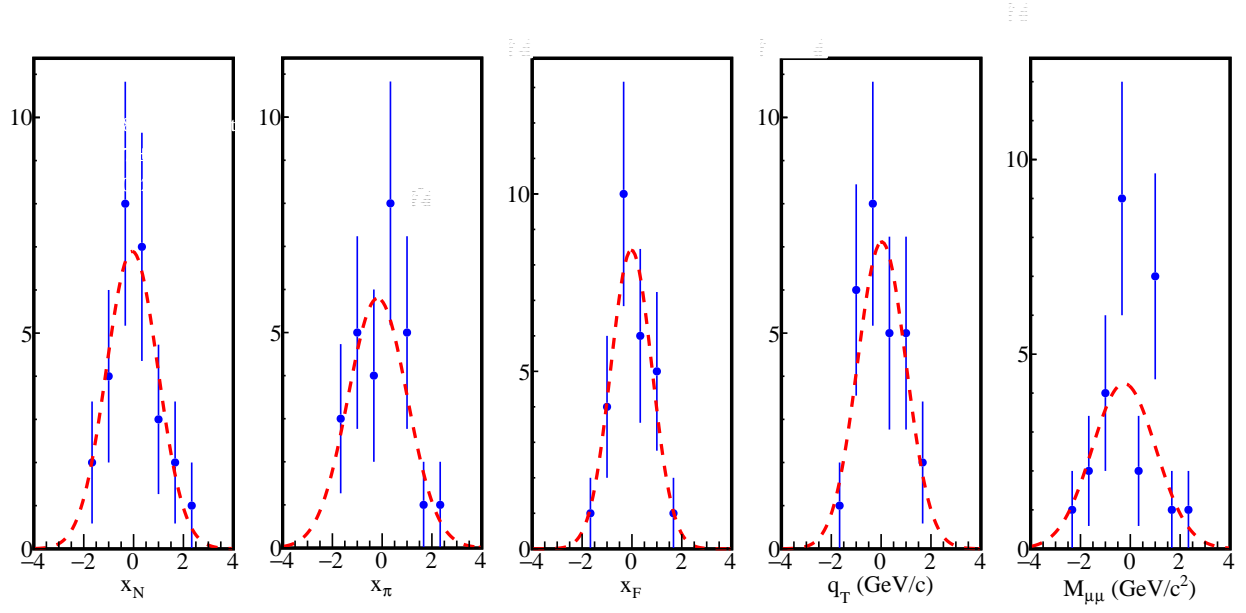


Figure 1.15: Uncorrelated pulls of the two target geomean false asymmetry

Entries	27	Entries	27	Entries	27	Entries	27	Entries	27
$\chi^2 / \text{ndf}$	1.06 / 4	$\chi^2 / \text{ndf}$	2.875 / 4	$\chi^2 / \text{ndf}$	1.203 / 3	$\chi^2 / \text{ndf}$	1.925 / 3	$\chi^2 / \text{ndf}$	7.364 / 5
Constant	$6.898 \pm 2.019$	Constant	$5.797 \pm 1.578$	Constant	$8.419 \pm 2.089$	Constant	$7.116 \pm 1.826$	Constant	$4.248 \pm 1.307$
Mean	$-0.05617 \pm 0.22189$	Mean	$-0.1796 \pm 0.3545$	Mean	$-0.02243 \pm 0.17361$	Mean	$0.0256 \pm 0.2382$	Mean	$-0.2528 \pm 0.3265$
Sigma	$1.032 \pm 0.266$	Sigma	$1.187 \pm 0.317$	Sigma	$0.8256 \pm 0.1377$	Sigma	$0.9721 \pm 0.1962$	Sigma	$1.279 \pm 0.331$

Figure 1.16: Gaussian fit results for the uncorrelated two target false geomean pulls

This false asymmetry can also be thought of as measuring the normalized counts on the Jura side minus the Saleve side but for each target individually. Both this false asymmetry and the previous false asymmetry can be written as Eq. 1.18 where  $\alpha$  will be an acceptance ratio of Jura/Saleve. As the Jura/Saleve acceptance ratio is expected to be the same for the upstream and downstream targets, any difference between the two false asymmetries must be due to other reasons. A by period comparison between the upstream and downstream target is shown in Fig. 1.17 and as can be seen there are difference by period between the upstream and downstream asymmetries. A combined pull

distribution is made using the information from both upstream and downstream asymmetries and is shown in Fig. 1.18. As with the previous false asymmetry, lack of data leads to the same problems with fit and therefore the same weighting method is used to determine a systematic error.

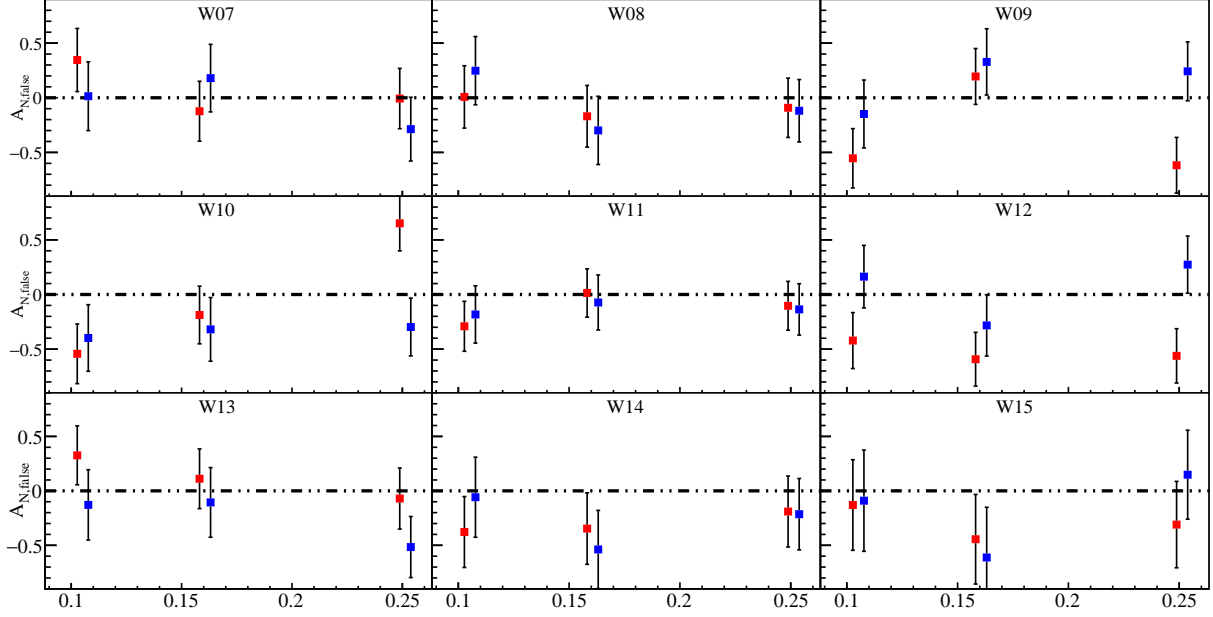


Figure 1.17: One target false asymmetries for the upstream target (red) and the downstream target (blue), as a function of  $x_N$ . Each graph is from a different period in time.

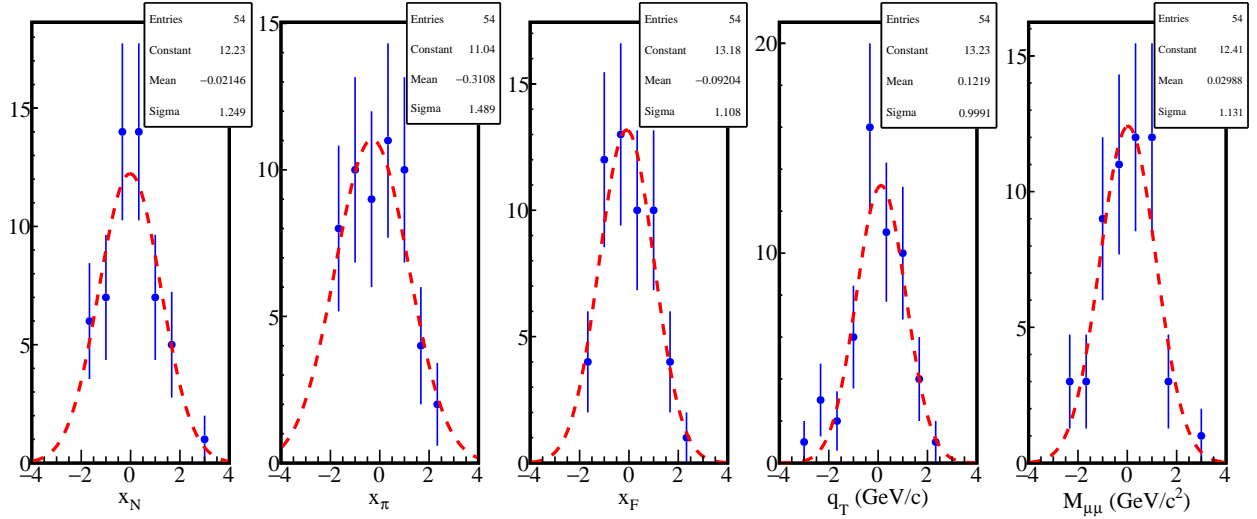


Figure 1.18: Pull values from one target geomean false asymmetries. Both upstream and downstream values are used to make this pull

3. Finally the same false asymmetry used to determine the acceptance fluctuations, Eq. 1.17, is also

checked for compatibility and a systematic error is determined in the same way as the previous false asymmetries. The pulls are shown in Fig. 1.19 and the corresponding fit parameters are shown in Fig. 1.20.

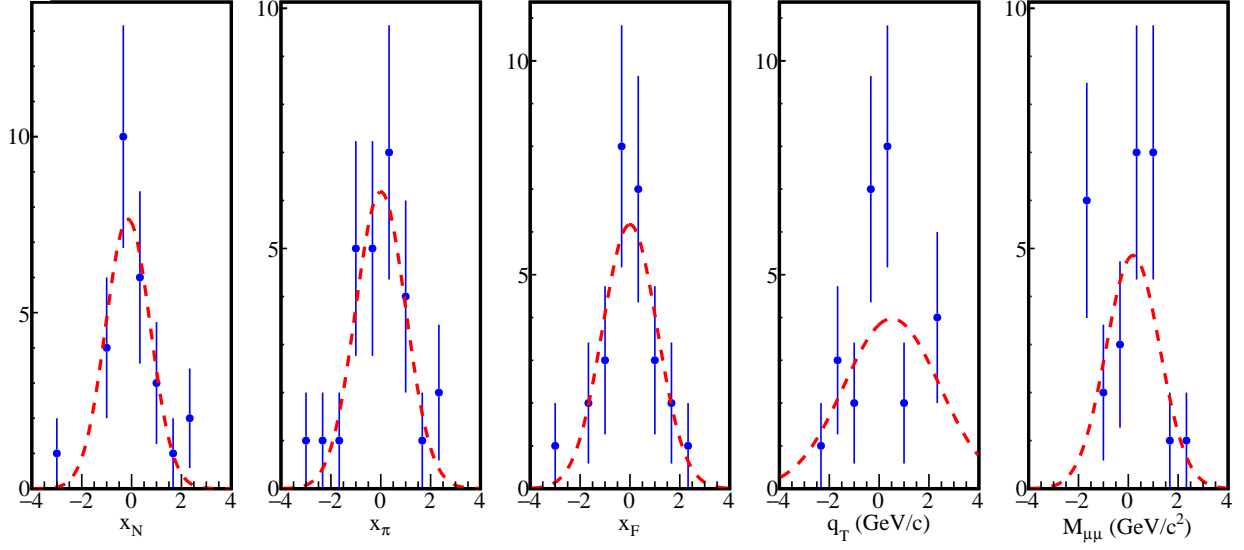


Figure 1.19: Pull distribution for a nearly acceptance free two target false geomean asymmetry

Entries	27	Entries	27	Entries	27	Entries	27	Entries	27
$\chi^2 / \text{ndf}$	3.517 / 4	$\chi^2 / \text{ndf}$	3.737 / 6	$\chi^2 / \text{ndf}$	2.357 / 5	$\chi^2 / \text{ndf}$	6.734 / 4	$\chi^2 / \text{ndf}$	7.973 / 4
Constant	$7.658 \pm 3.014$	Constant	$6.183 \pm 1.859$	Constant	$6.176 \pm 2.115$	Constant	$3.971 \pm 1.201$	Constant	$4.857 \pm 4.667$
Mean	$-0.1441 \pm 0.2765$	Mean	$-0.002351 \pm 0.211941$	Mean	$-0.002406 \pm 0.246275$	Mean	$0.5095 \pm 1.1086$	Mean	$0.1882 \pm 0.9446$
Sigma	$0.891 \pm 0.424$	Sigma	$1.004 \pm 0.226$	Sigma	$1.098 \pm 0.361$	Sigma	$1.92 \pm 1.12$	Sigma	$1.072 \pm 1.195$

Figure 1.20: Gaussian fit results for the previous pull distributions

A summary of the systematic error from each false asymmetry is shown in Tab. 1.5

Systematic error	$\langle\sigma_{\text{systematic}}/\sigma_{\text{statistical}}\rangle$
Two target Jura-Saleve	0.26
Combined one target	0.5
Two target acceptance estimation	0.29

Table 1.5: Summary of systematic error impacts from false asymmetries. The maximum systematic error is chosen as the systematic error.

#### 1.4.4 Left/Right Event Migration

The spectrometer has finite resolution for any measured quantity and for this reason events measured as left outgoing could really be events that are right outgoing and vice versa for measured left outgoing events. This left-right miss-identification has the result of diluting spin-dependent effects by effectively having a sample from an unpolarized target along with the sample from the polarized target. Therefore the asymmetry  $A_N$  reduces from left-right miss-identification and this effect is included as a systematic effect.

For this thesis five Monte-Carlo processes were generated corresponding to three background processes and a spin-independent signal process. The generator used was PHTHYIA8 and the data was generated and reconstruction at Blue Waters. The background processes simulated were J $\Psi$ i production,  $\Psi$ i' production and open charm (OC) production. Each of these backgrounds can decay into two muons which results in a background contamination to the Drell-Yan signal. Table ?? gives the parameters used for the Monte-Carlo studied.

Table 1.6: Monte-Carlo settings produced on Blue Waters

Event generator	PYTHIA8
Pion pdf	GRVPI1
Proton pdf	NNPDF23
proton/neutron mixing ratio	1.96
Initial state radiation	on
Final state radiation	on
Multiple parton interactions	on
Simulated detector efficiencies	uniform

Miss-identification was estimated from the simulated Monte-Carlo data sample described in Table ?? where the sample was made from the respond of the COMPASS spectrometer to input Drell-Yan events in a similar mass range. The same analysis performed on real data was performed on this Monte-Carlo data to get the angles of interest. Fig. 1.21 shows the rate of events identified correctly and incorrectly as a function of the  $\phi_s$ . This plot is made by determining which outgoing direction the generated events emerged with the outgoing direction the reconstructed events emerged.

As is clearly visible there is a band of higher miss-identification rate at the border between left and right.

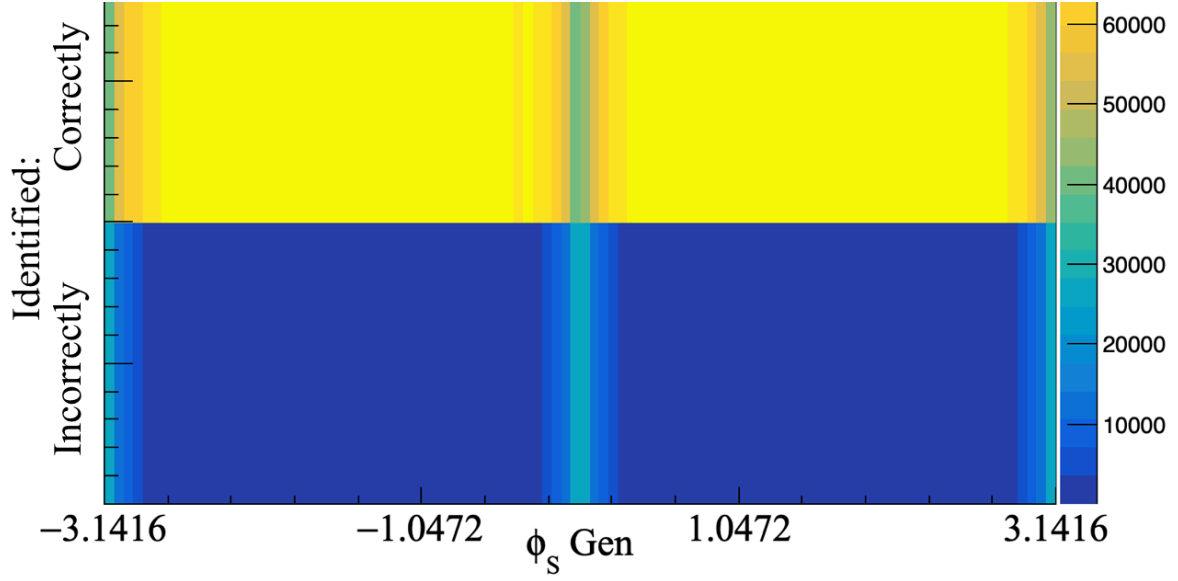


Figure 1.21: The rate of identified correctly and incorrectly left-right events as a function of  $\phi_S$ . This is determined by comparing the generated outgoing direction with the reconstructed outgoing direction. The left-right boundary is clearly visible at  $\phi_S = 0^\circ$  and  $\phi_S = -\pi^\circ$  and  $\phi_S = \pi^\circ$

For this reason a cut in the  $\phi_S$  variable symmetric about the left-right border was tested to determine the percent of miss-identification as a function of the amount of  $\phi_S$  cut. These results are shown in Fig. 1.22.

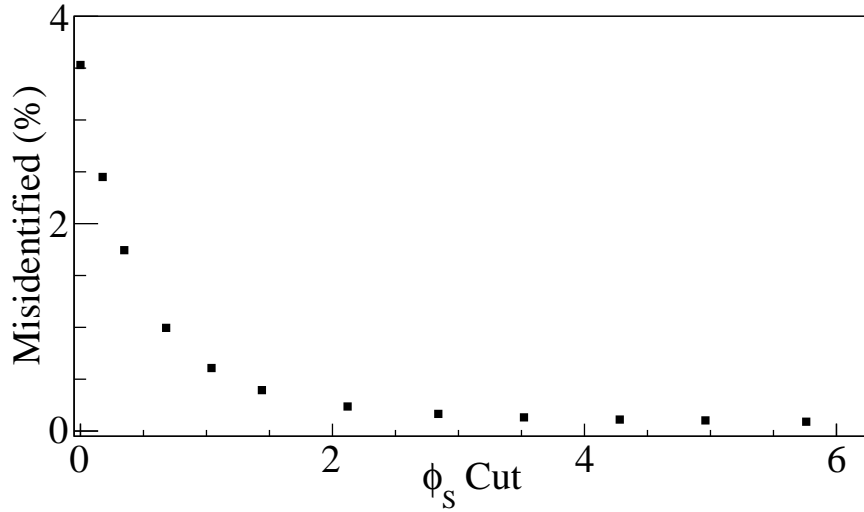


Figure 1.22: Percent left-right migration as a function of the amount of  $\phi_S$  cut.

The systematic error for left-right migration is calculated as



$$\delta A_{N,\text{systematic}} = \gamma * A_N + \gamma * \delta A_N, \quad (1.24)$$

where this expression is derived in Appendix ??.

No cut on  $\phi_S$  was used for the asymmetry due to the fact that the systematic error is already small with no cut in  $\phi_S$  and to avoid loss of statistics. The integrated systematic error due to left-right event migration was determined to be 9%.

### 1.4.5 Total Systematics

The total systematic error is determined by adding all non-zero systematic effects in quadrature as

$$\left\langle \frac{\sigma_{\text{systematics}}}{\sigma_{\text{statistical}}} \right\rangle = \sqrt{\sum_i^{\text{all systematics}} \left\langle \frac{\sigma_{\text{systematics},i}^2}{\sigma_{\text{statistical}}^2} \right\rangle}, \quad (1.25)$$

where all the systematic effects considered are summarized in Tab. 1.7.

Systematic error	$\langle \sigma_{\text{systematic}} / \sigma_{\text{statistical}} \rangle$	$\langle \sigma_{\text{systematic}} \rangle$	$\langle \sigma_{\text{statistical}} \rangle$
Period compatibility	0.0	0.0	0.039
Acceptance fluctuation	0.2	0.008	0.039
False asymmetry	0.5	0.020	0.039
Left-Right migration	0.09	0.004	0.039
Total	0.55	0.021	0.039

Table 1.7: Summary of systematic error impacts to the integrated asymmetry

## 1.5 Results

(need to explain way polarization is corrected by period)

The asymmetries in this analysis are extracted separately from each of the nine data periods, Table 1.1, and then combined as a weighted average. This calculation method is used to minimize the effects of acceptance changes between periods as the spectrometer was kept stable within each period but had the options for detector changes and repairs between periods. This resulting asymmetry,  $A_N$  for each method, section 1.3.1 and section 1.3.2, is determined from a weighted average as

$$A_N = \frac{\sum_{\text{period}} A_{N,\text{period}} \sigma_{\text{period}}^{-2}}{\sum_{\text{period}} \sigma_{\text{period}}^{-2}}, \quad \delta A_N = \sqrt{\sum_{\text{period}} \frac{1}{\sigma_{\text{period}}^{-2}}}. \quad (1.26)$$

The results for the basic geometric mean are shown in Fig. 1.23 and the results for the two target geometric

mean are shown in Fig. 1.24. The numerical values for the two-target geometric mean with statistical and systematic error bars are summarized in Table ???. The systematic error bars are discussed in Sec. 1.4.

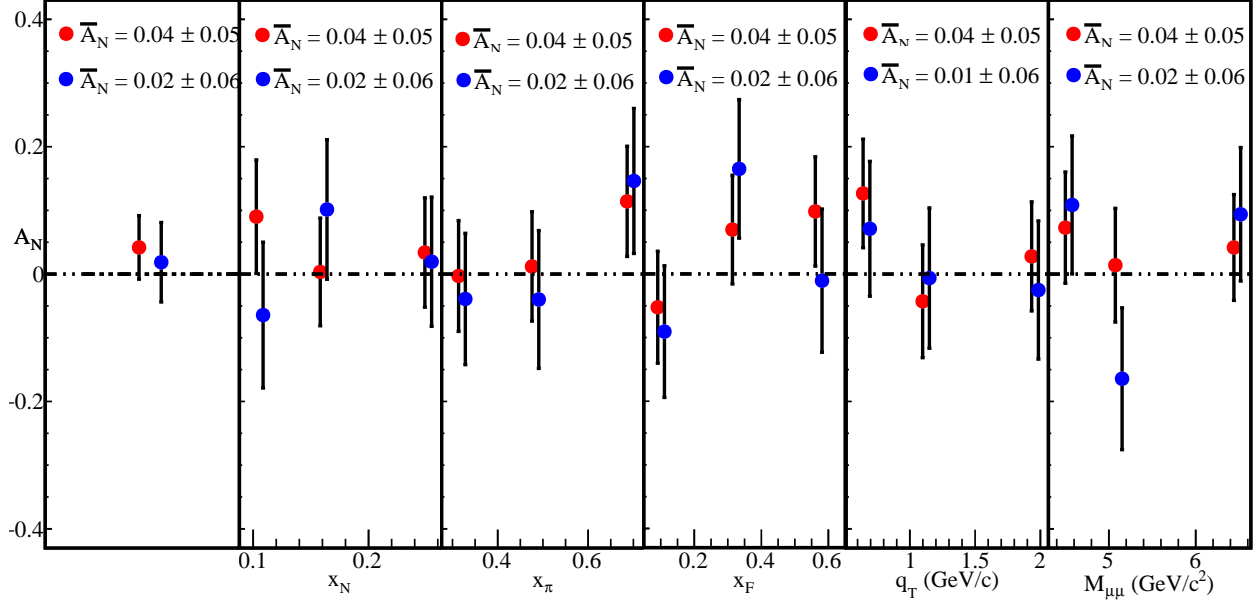


Figure 1.23:  $A_N$  determined from the geometric mean method for the upstream target (red) and the downstream target (blue) for all kinematic binnings

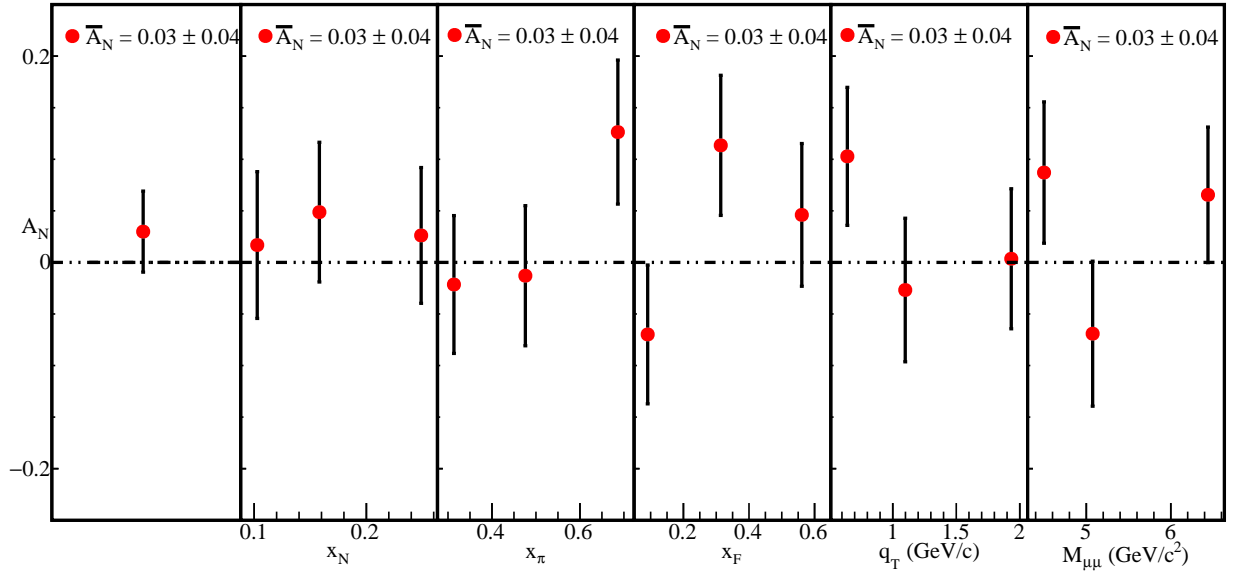


Figure 1.24:  $A_N$  determined by the two-target geometric mean method for all kinematic binnings

Table 1.8: Two-Target geometric mean numerical values and error bars for each kinematic bin

Binning variable	Bin Range	$A_N$	$\delta A_N^{\text{stat}}$	$\delta A_N^{\text{sys}}$
$\langle x_N \rangle$				

### 1.5.1 Comparison of results

# References

- [1] M. Aghasyan et al. First measurement of transverse-spin-dependent azimuthal asymmetries in the Drell-Yan process. *Phys. Rev. Lett.*, 119(11):112002, 2017. doi: 10.1103/PhysRevLett.119.112002.
- [2] M. Anselmino, M. Boglione, U. D'Alesio, F. Murgia, and A. Prokudin. Study of the sign change of the Sivers function from STAR Collaboration W/Z production data. *JHEP*, 04:046, 2017. doi: 10.1007/JHEP04(2017)046.
- [3] Miguel G. Echevarria, Ahmad Idilbi, Zhong-Bo Kang, and Ivan Vitev. QCD Evolution of the Sivers Asymmetry. *Phys. Rev.*, D89:074013, 2014. doi: 10.1103/PhysRevD.89.074013.
- [4] Peng Sun and Feng Yuan. Transverse momentum dependent evolution: Matching semi-inclusive deep inelastic scattering processes to Drell-Yan and W/Z boson production. *Phys. Rev.*, D88(11):114012, 2013. doi: 10.1103/PhysRevD.88.114012.